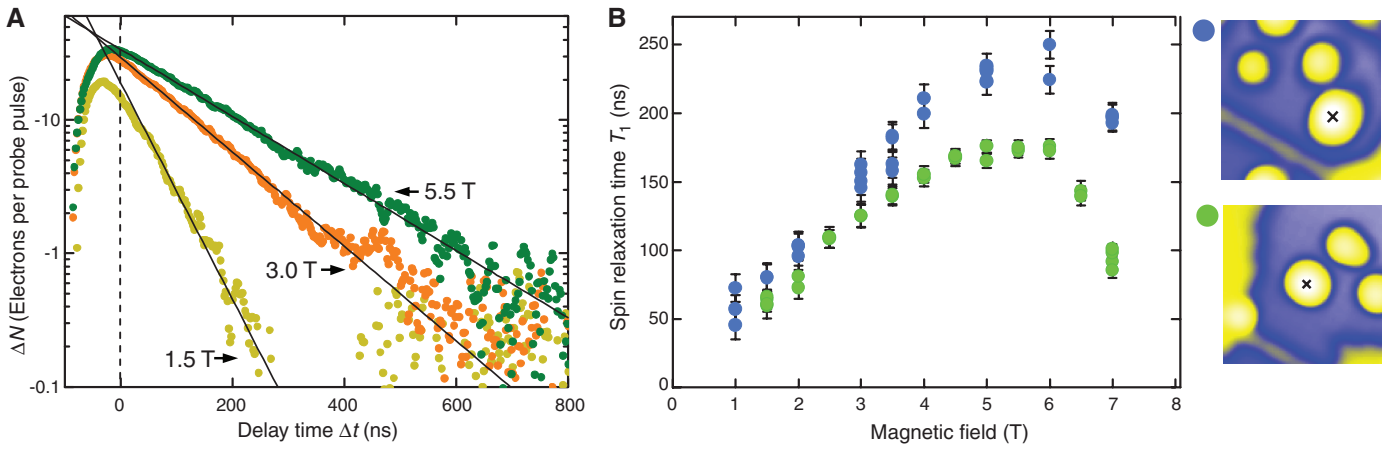

Fig. 4. Field and site dependence of the spin relaxation time. (**A**) Pump-probe measurements for different magnetic fields on an Fe-Cu dimer; solid lines are exponential fits. (**B**) T_1 as a function of magnetic field for the two Fe-Cu dimers shown in the accompanying 5-nm by 5-nm STM topographs.

One of the Fe-Cu dimers in Fig. 4B always exhibits a larger T_1 than the other. We speculate that this variation is due to differences in the nearby surface features as seen in the accompanying topographs. This observation emphasizes the capability of the all-electronic pump-probe technique presented here to resolve local variations in the spin relaxation time with atomic precision.

The pump-probe scheme we have described can be used to monitor the temporal evolution of any excitation provided (i) the excitation can be driven by tunneling electrons; (ii) the conductance of the tunnel junction exhibits a postexcitation time dependence; and (iii) the system evolves on an accessible time scale. Excitations fulfilling these requirements include long-lived vibrational excitations, conformational changes of molecules (*26*) such as in molecular motors (*27*), or fast localized heating (*28*). We emphasize that this pump-probe scheme can in principle be used to monitor the dynamical evolution of the excited state, not just its relaxation; with sufficient temporal resolution it should be possible to monitor the vibration of an atom or molecule and even the precession of a spin.

References and Notes

1. C. P. Slichter, *Principles of Magnetic Resonance* (Springer, Berlin and New York, 1996).
2. D. Rugar, R. Budakian, H. J. Mamin, B. W. Chui, *Nature* **430**, 329 (2004).
3. J. R. Maze *et al.*, *Nature* **455**, 644 (2008).
4. G. Balasubramanian *et al.*, *Nature* **455**, 648 (2008).
5. M. Bode *et al.*, *Nature* **447**, 190 (2007).
6. A. J. Heinrich, J. A. Gupta, C. P. Lutz, D. M. Eigler, *Science* **306**, 466 (2004).
7. N. Tsukahara *et al.*, *Phys. Rev. Lett.* **102**, 167203 (2009).
8. C. F. Hirjibehedin *et al.*, *Science* **317**, 1199 (2007).
9. X. Chen *et al.*, *Phys. Rev. Lett.* **101**, 197208 (2008).
10. C. F. Hirjibehedin, C. P. Lutz, A. J. Heinrich, *Science* **312**, 1021 (2006).
11. M. J. Rost *et al.*, *Rev. Sci. Instrum.* **76**, 053710 (2005).
12. C. Durkan, M. E. Welland, *Appl. Phys. Lett.* **80**, 458 (2002).
13. G. Nunes Jr., M. R. Freeman, *Science* **262**, 1029 (1993).
14. O. Takeuchi *et al.*, *Appl. Phys. Lett.* **85**, 3268 (2004).
15. S. Loth *et al.*, *Nat. Phys.* **6**, 340 (2010).
16. R. Wiesendanger, *Rev. Mod. Phys.* **81**, 1495 (2009).
17. Materials and methods are available as supporting material on *Science* Online.
18. M. N. Leuenberger, D. Loss, *Nature* **410**, 789 (2001).
19. D. E. Freedman *et al.*, *J. Am. Chem. Soc.* **132**, 1224 (2010).
20. A. Ardavan *et al.*, *Phys. Rev. Lett.* **98**, 057201 (2007).
21. T. Choi, C. D. Ruggiero, J. A. Gupta, *Phys. Rev. B* **78**, 035430 (2008).
22. F. Komori, S.-Y. Ohno, K. Nakatsuji, *Prog. Surf. Sci.* **77**, 1 (2004).
23. D. Gatteschi, R. Sessoli, J. Villain, *Molecular Nanomagnets* (Oxford Univ. Press, New York, 2006).
24. C. Sangregorio, T. Ohm, C. Paulsen, R. Sessoli, D. Gatteschi, *Phys. Rev. Lett.* **78**, 4645 (1997).
25. W. Wernsdorfer, R. Sessoli, *Science* **284**, 133 (1999).
26. K. Henzler-Wildman, D. Kern, *Nature* **450**, 964 (2007).
27. W. R. Browne, B. L. Feringa, *Nat. Nanotechnol.* **1**, 25 (2006).
28. B. Barwick, H. S. Park, O.-H. Kwon, J. S. Baskin, A. H. Zewail, *Science* **322**, 1227 (2008).
29. J. A. Gupta, C. P. Lutz, A. J. Heinrich, D. M. Eigler, *Phys. Rev. B* **71**, 115416 (2005).

30. We thank B. Melior for technical assistance. S.L., C.P.L., and A.J.H. acknowledge financial support from the Office of Naval Research, S.L. from the Alexander von Humboldt Foundation, and M.E. from European Science Foundation project FunSMARTs II.

Supporting Online Material

www.sciencemag.org/cgi/content/full/329/5999/1628/DC1
Materials and Methods
Figs. S1 to S3
References
Movie S1

30 April 2010; accepted 4 August 2010
10.1126/science.1191688

Optical Clocks and Relativity

C. W. Chou,* D. B. Hume, T. Rosenband, D. J. Wineland

Observers in relative motion or at different gravitational potentials measure disparate clock rates. These predictions of relativity have previously been observed with atomic clocks at high velocities and with large changes in elevation. We observed time dilation from relative speeds of less than 10 meters per second by comparing two optical atomic clocks connected by a 75-meter length of optical fiber. We can now also detect time dilation due to a change in height near Earth's surface of less than 1 meter. This technique may be extended to the field of geodesy, with applications in geophysics and hydrology as well as in space-based tests of fundamental physics.

Albert Einstein's theory of relativity forced us to alter our concepts of reality. One of the more startling outcomes of the theory is that we have to give up our notions of simultaneity. This is manifest in the so-called twin paradox (*1*), in which a twin sibling who travels on a fast-moving rocket ship returns home younger than the other twin. This "time dilation" can be quantified by comparing the tick rates of identical clocks that accompany the traveler and the stationary observer. Another consequence of Einstein's theory is that clocks run more slowly near massive objects. In the range of speeds and length scales encountered in our daily life, relativistic effects are extremely small. For example, if two identical clocks are separated vertically by 1 km near the surface of Earth, the higher clock emits about three more second-ticks than the lower one in a million years. These effects of relativistic time dilation have been verified in several important experiments (*2*–*6*)

Time and Frequency Division, National Institute of Standards and Technology (NIST), Boulder, CO 80305, USA.

*To whom correspondence should be addressed. E-mail: chinwen@nist.gov

and are accounted for routinely in satellite-based navigation systems (*7*). The most accurate determinations historically involve velocities near the speed of light (*8*) and changes in elevation of 10^4 to 10^7 m (*3*, *4*). Previously, small relativistic shifts ($<10^{-16}$) could be observed only over short distances in γ-ray Mössbauer spectroscopy (*5*, *9*) and atom interferometry (*6*). However, they might be detected over longer distances by clocks with sufficiently high sensitivity, such as accurate atomic clocks operating in the optical regime, or "optical clocks." Here we report the detection of relativistic time dilation due to velocities of several meters per second and, separately, due to a change in height of 0.33 m by comparing two optical clocks based on $^{27}Al^+$ ions.

With operating frequencies in the petahertz (1 PHz = 10^{15} Hz) range and natural linewidths at the millihertz level, optical clocks have demonstrated substantial improvements in stability and accuracy over the current microwave time and frequency standards (*10*). We compared two optical atomic clocks based on individual trapped Al^+ ions, with reported systematic frequency uncertainties of 8.6×10^{-18} (*11*) and 2.3×10^{-17} (*12*). For comparison, the lowest reported frequency uncertainty of Cs fountain clocks is 3.4×10^{-16} (*13*). With the accuracy and the associated sensitivity of these Al^+ optical clocks, frequency variations below 10^{-16} in the clocks due to relativistic effects can be observed.

Due to the lack of an accessible optical transition in $^{27}Al^+$ for efficient laser cooling and state detection, precision spectroscopy of these ions uses techniques developed in quantum information science. Here, an Al^+ ion is sympathetically cooled through its Coulomb interaction with an auxiliary "logic" ion that is simultaneously held in the same linear radio-frequency (RF) Paul trap (*14*). The logic ion also helps prepare and detect the internal state of the Al^+ ion via quantum logic protocols. In this work, the two Al^+ clocks used a beryllium ($^9Be^+$) ion (*14*) and a magnesium ($^{25}Mg^+$) ion (*11*), respectively, as the logic ion. The Al^+ $^1S_0 \leftrightarrow {}^3P_0$ clock transition with frequency f_0 near 1.121 PHz has a narrow (Δf = 8 mHz) natural linewidth and a corresponding intrinsic quality (Q) factor of $f_0/\Delta f = 1.4 \times 10^{17}$ that permits high sensitivity for detecting small frequency-shifting effects. However, the observed linewidth for the clock transition is limited by the linewidth of the probe laser. We probed the clock transition with a subhertz linewidth laser referenced to a high-finesse optical cavity (*15*). In the Al-Mg clock, with 300 ms probe duration we obtained a narrow, Fourier transform–limited linewidth, realizing a Q factor of 4.2×10^{14} with nearly 80% contrast (Fig. 1). This high-Q line provides the basis for high-stability clock operation and sensitivity to small frequency shifts.

The two Al^+ optical clocks were located in separate laboratories and were compared by transmitting the stable clock signal through a 75-m length of phase-stabilized optical fiber. To observe time dilation due to motion, we set the Al^+ ion in the Al-Mg clock in motion by applying a small static electric field that shifts the position of the ion slightly away from the null of the confining RF field (*16*). The ion is thereby subject to an RF electric field at f_{RF} = 59 MHz (Fig. 2) and undergoes harmonic motion. The ion velocity is adjusted by varying the applied static electric field. In the language of the twin paradox, the moving Al^+ ion is the traveling twin, and its harmonic motion amounts to many round trips. Time dila-

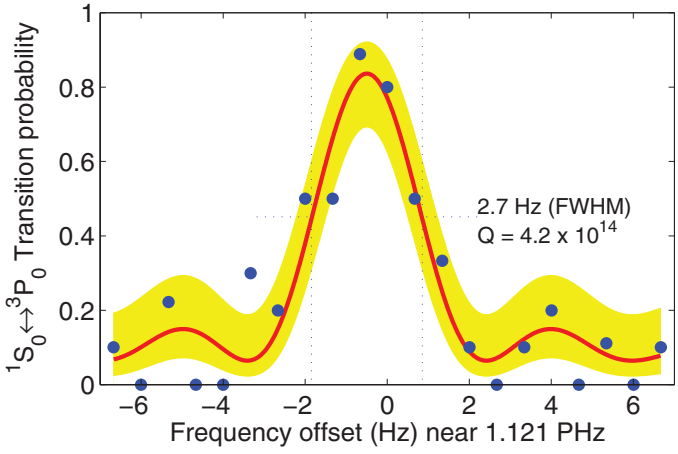

Fig. 1. The $^1S_0 \leftrightarrow {}^3P_0$ transition in Al^+ observed with probe pulses of 300 ms duration. Each datum (blue dots) consists of an average of 9 or 10 individual probes, and the sequence of probe frequencies was randomized to eliminate skewing effects due to frequency drifts in the probe laser. A Lorentzian fit to this data (not shown in the figure) produces a linewidth [full width at half maximum (FWHM)] of 2.30 ± 0.51 Hz (uncertainties correspond to 1 SD). The Lorentzian linewidth is narrower than the Fourier transform–limited spectrum (smooth fitted red curve) that is the result of the rectangular temporal waveform of the probe pulses. For the probe time used here, the Fourier limit corresponds to a linewidth (FWHM) of 2.7 Hz and a Q factor of 4.2×10^{14}, which we take as the achieved values. The yellow shaded band indicates the expected scatter of the data due to quantum projection noise (*34*).

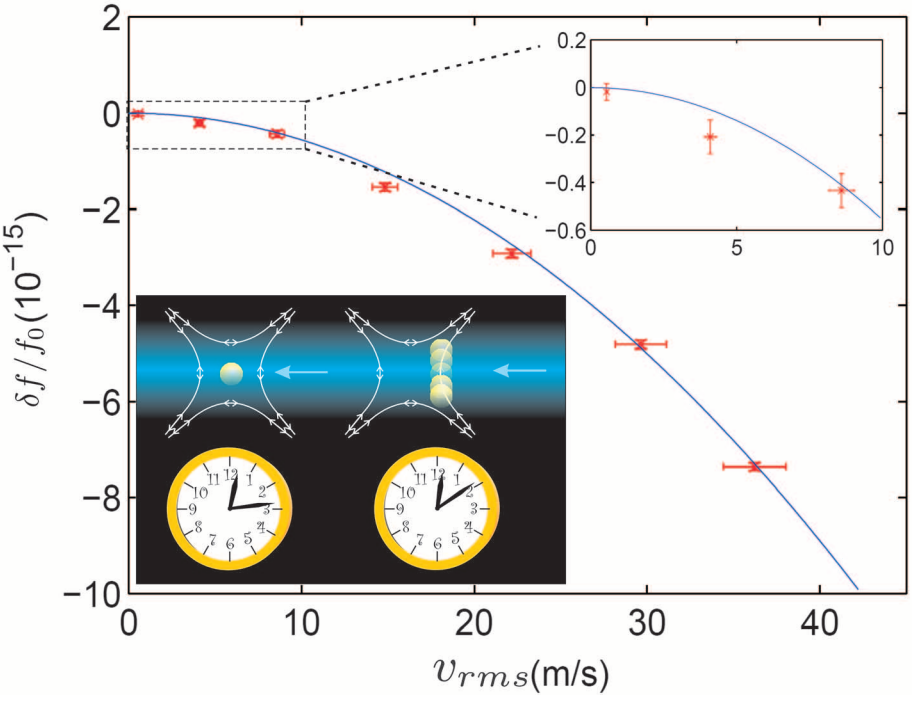

Fig. 2. Relativistic time dilation at familiar speeds (10 m/s = 36 km/hour ≈ 22.4 miles/hour). (Lower left inset) As the Al^+ ion in one of the twin clocks is displaced from the null of the confining RF quadrupole field (white field lines), it undergoes harmonic motion and experiences relativistic time dilation. In the experiments, the motion is approximately perpendicular to the probe laser beam (indicated by the blue shading). The Al^+ ion clock in motion advances at a rate that is slower than its rate at rest. In the figure, the fractional frequency difference between the moving clock and the stationary clock is plotted versus the velocity ($v_{rms} = \sqrt{\langle v^2 \rangle}$) (rms, root mean square) of the moving clock. The solid curve represents the theoretical prediction. (Upper right inset) A close-up of the results for $v_{rms} < 10$ m/s in the dashed box. The vertical error bars represent statistical uncertainties, and the horizontal ones cover the spread of measured velocities at the applied electric fields.

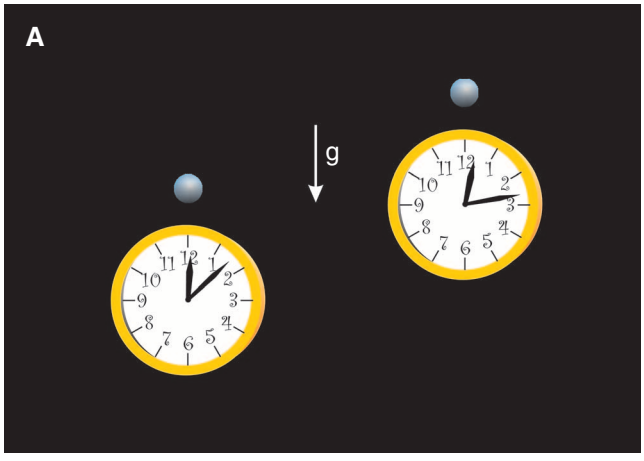

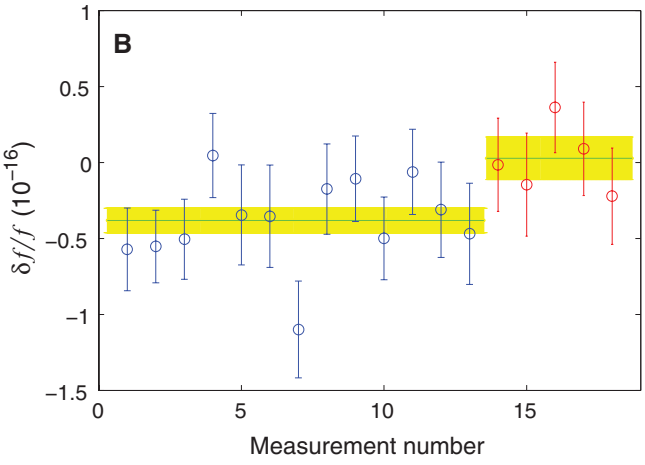

Fig. 3. Gravitational time dilation at the scale of daily life. (**A**) As one of the clocks is raised, its rate increases when compared to the clock rate at deeper gravitational potential. (**B**) The fractional difference in frequency between two Al^+ optical clocks at different heights. The Al-Mg clock was initially 17 cm lower in height than the Al-Be clock, and subsequently, starting at data point 14, elevated by 33 cm. The net relative shift due to the increase in height is measured to be $(4.1 \pm 1.6) \times 10^{-17}$. The vertical error bars represent statistical uncertainties (reduced $\chi^2 = 0.87$). Green lines and yellow shaded bands indicate, respectively, the averages and statistical uncertainties for the first 13 data points (blue symbols) and the remaining 5 data points (red symbols). Each data point represents about 8000 s of clock-comparison data.

tion from this motion leads to a fractional frequency shift for the moving clock of (*17*)

$$\frac{\delta f}{f_0} = \frac{1}{\langle \gamma(1 - v_\parallel/c)\rangle} - 1 \qquad (1)$$

Here $v_\parallel$ is the velocity of the Al^+ ion along the wave vector of the probe laser beam $\gamma = 1/\sqrt{1 - v^2/c^2}$, c is the speed of light, v is the ion's velocity with respect to the laboratory reference frame, and f_0 is the ion's proper resonant frequency. Angle brackets denote time averages. Because the induced Al^+ ion motion is harmonic, its contribution to $\langle v_\parallel \rangle$ averages to zero; therefore, any observed change in the ion's transition frequency is due to a change in γ and corresponds to relativistic time dilation (*18*). For $v/c << 1$, Eq. 1 can be approximated by $\delta f/f_0 \approx -\langle v^2\rangle/2c^2$ (*17*). We measured the frequency difference between the two clocks ($\delta f/f_0$) while varying the velocity of the ion motion. The experimental results, which confirm the prediction of Eq. 1, are plotted in Fig. 2.

Differences in gravitational potential can be detected by comparing the tick rate of two clocks. For small height changes on the surface of Earth, a clock that is higher by a distance Δh runs faster by

$$\frac{\delta f}{f_0} = \frac{g\Delta h}{c^2} \qquad (2)$$

where $g \approx 9.80$ m/s^2 is the local acceleration due to gravity (*4*). The gravitational shift corresponds to a clock shift of about 1.1×10^{-16} per meter of change in height. To observe this shift, we first compared the frequencies of the two Al^+ clocks at the original height difference of $\Delta h = h$(Mg-Al) − h(Be-Al) = −17 cm, which was measured with a laser level. Then we elevated the optical table on which the Mg-Al clock was mounted, supporting it on platforms that increased the height by 33 cm, and compared the frequencies again. The two measurements consist of approximately 100,000 s of low-height data and 40,000 s of high-height data, and the clocks exhibit (Fig. 3) a fractional frequency change of $(4.1 \pm 1.6) \times 10^{-17}$. When this shift is interpreted as a measurement of the change in height of the Al-Mg clock, the result of 37 ± 15 cm agrees well with the known value of 33 cm.

Although ideally $\langle v_\parallel \rangle = 0$, small linear velocities of the Al^+ ions can occur because of effects such as slow electrical charging of insulating material in the trap. From Eq. 1, the clock's frequency (that is, the frequency of the probe laser locked to the moving ion's clock transition) exhibits a fractional frequency shift

$$\frac{\delta f}{f_0} \approx \frac{\langle v_\parallel \rangle}{c} \qquad (3)$$

if the Al^+ ion is moving at an average velocity $\langle v_\parallel \rangle$ in the propagation direction of a probe laser beam. In the comparison measurements between the Al^+ clocks, the Doppler effect was carefully constrained by alternate use of probe laser beams counter-propagating with respect to each other (*11*). Any motion of the ion is detected as a difference in the transition frequencies measured by the two laser beams. In the Al-Mg clock, we observed a fractional frequency difference of $(1.2 \pm 0.7) \times 10^{-17}$ between the two probe directions, which corresponds to the ion moving at a speed of (1.8 ± 1.1) nm/s in the lab frame. However, the clock rate is not significantly affected by a velocity of this magnitude, because it is derived from an average of the two opposite laser-probe directions.

Small relativistic effects reported here have been observed with optical atomic clocks of unprecedented precision and accuracy. With improved accuracy, the sensitivity of optical clocks to small variations in gravitational potential might find applications in geodesy (*19*, *20*), hydrology (*21*), and tests of fundamental physics in space (*22*). The basic components for clock-based geodetic measurements were demonstrated here by comparing two accurate Al^+ optical clocks through 75 m of noise-canceled fiber and measuring height-dependent clock shifts. In clock-based geodesy (*23*, *24*), accurate optical clocks would be linked to form a network of "inland tide gauges" (*25*) that measure the distance from Earth's surface to the geoid: the equipotential surface of Earth's gravity field that matches the global mean sea level. Such a network could operate with high temporal (daily) and geospatial resolution at the clock locations. It would therefore complement geodetic leveling networks, whose update period is typically 10 years or longer, as well as biweekly satellite-generated global geoid maps.

For a network to be useful, clock accuracy must be improved to 10^{-18} or better (*26*–*28*) to allow for height measurements with 1-cm uncertainty. In Al^+ clocks, improved control of the ion motion is needed to reduce the uncertainty of motional time dilation, and issues of reliability must be addressed, so that the clocks can operate unattended for long periods. High-quality links are also needed to connect the optical clocks. Realistic link demonstrations with telecommunications fiber akin to the links used in this work have shown that optical frequencies can be transmitted across fiber lengths of up to 250 km with inaccuracy below 10^{-18} (*29*–*31*), and continent-scale demonstrations are in progress (*30*). However, intercontinental links may require the faithful transmission of optical carrier frequencies to satellites through the atmosphere, and this is an unsolved problem under active investigation (*32*, *33*).

References and Notes

1. A. Einstein, *Annal. Physik* **17**, 891 (1905).
2. B. Rossi, D. B. Hall, *Phys. Rev.* **59**, 223 (1941).
3. J. C. Hafele, R. E. Keating, *Science* **177**, 166 (1972).
4. R. F. C. Vessot *et al.*, *Phys. Rev. Lett.* **45**, 2081 (1980).

5. R. V. Pound, G. A. Rebka, *Phys. Rev. Lett.* **4**, 337 (1960).
6. H. Müller, A. Peters, S. Chu, *Nature* **463**, 926 (2010).
7. N. Ashby, M. Weiss, *NIST Technical Note 1385* (NIST, Boulder, CO, 1999).
8. S. Reinhardt *et al.*, *Nat. Phys.* **3**, 861 (2007).
9. W. Potzel *et al.*, *Hyperfine Interact.* **72**, 195 (1992).
10. P. Gill, *Metrologia* **42**, S125 (2005).
11. C. W. Chou, D. B. Hume, J. C. J. Koelemeij, D. J. Wineland, T. Rosenband, *Phys. Rev. Lett.* **104**, 070802 (2010).
12. T. Rosenband *et al.*, *Science* **319**, 1808 (2008).
13. T. E. Parker, *Metrologia* **47**, 1 (2010).
14. P. O. Schmidt *et al.*, *Science* **309**, 749 (2005).
15. B. C. Young, F. C. Cruz, W. M. Itano, J. C. Bergquist, *Phys. Rev. Lett.* **82**, 3799 (1999).
16. D. J. Berkeland, J. D. Miller, J. C. Bergquist, W. M. Itano, D. J. Wineland, *J. Appl. Phys.* **83**, 5025 (1998).
17. See supporting material on *Science* Online.
18. D. Hasselkamp, E. Mondry, A. Scharmann, *Z. Physik A* **289**, 151 (1979).
19. D. Kleppner, *Phys. Today* **59**, 10 (2006).
20. B. D. Tapley, S. Bettadpur, J. C. Ries, P. F. Thompson, M. M. Watkins, *Science* **305**, 503 (2004).
21. R. Schmidt *et al.*, *Surv. Geophys.* **29**, 319 (2008).
22. G. Tino *et al.*, *Nucl. Phys. B Proc. Suppl.* **166**, 159 (2007).
23. A. Bjerhammar, *Bull. Geod.* **59**, 207 (1985).
24. J. Müller, M. Soffel, S. A. Klioner, *J. Geod.* **82**, 133 (2008).
25. O. Colombo, *Rep. No. 296* (Department of Geodetic Science, Ohio State University, Columbus, OH, 1980).
26. H. G. Dehmelt, *IEEE Trans. Instrum. Meas.* **31**, 83 (1982).
27. D. J. Wineland, W. M. Itano, J. C. Bergquist, R. G. Hulet, *Phys. Rev. A* **36**, 2220 (1987).
28. M. Takamoto, H. Katori, S. I. Marmo, V. D. Ovsiannikov, V. G. Pal'chikov, *Phys. Rev. Lett.* **102**, 063002 (2009).
29. N. R. Newbury, P. A. Williams, W. C. Swann, *Opt. Lett.* **32**, 3056 (2007).
30. G. Grosche *et al.*, *Opt. Lett.* **34**, 2270 (2009).
31. F. Kéfélian *et al.*, *Opt. Lett.* **34**, 1573 (2009).
32. B. Sprenger, J. Zhang, Z. H. Lu, L. J. Wang, *Opt. Lett.* **34**, 965 (2009).
33. K. Djerroud *et al.*, *Opt. Lett.* **35**, 1479 (2010).
34. W. M. Itano *et al.*, *Phys. Rev. A* **47**, 3554 (1993).

35. This work was supported by the Office of Naval Research and NIST. We thank N. Pavlis and M. Weiss for helpful discussions and J. C. Bergquist and N. Ashby for suggestions on the manuscript. Not subject to U.S. copyright.

Supporting Online Material

www.sciencemag.org/cgi/content/full/329/5999/1630/DC1
Methods
References

24 May 2010; accepted 5 August 2010
10.1126/science.1192720

Alkali-Stabilized Pt-OH_x Species Catalyze Low-Temperature Water-Gas Shift Reactions

Yanping Zhai,[1] Danny Pierre,[1]* Rui Si,[1]† Weiling Deng,[1]‡ Peter Ferrin,[2] Anand U. Nilekar,[2] Guowen Peng,[2] Jeffrey A. Herron,[2] David C. Bell,[3] Howard Saltsburg,[1] Manos Mavrikakis,[2]§ Maria Flytzani-Stephanopoulos[1]§

We report that alkali ions (sodium or potassium) added in small amounts activate platinum adsorbed on alumina or silica for the low-temperature water-gas shift (WGS) reaction ($H_2O + CO \rightarrow H_2 + CO_2$) used for producing H_2. The alkali ion–associated surface OH groups are activated by CO at low temperatures (~100°C) in the presence of atomically dispersed platinum. Both experimental evidence and density functional theory calculations suggest that a partially oxidized Pt-alkali-$O_x(OH)_y$ species is the active site for the low-temperature Pt-catalyzed WGS reaction. These findings are useful for the design of highly active and stable WGS catalysts that contain only trace amounts of a precious metal without the need for a reducible oxide support such as ceria.

The water-gas shift (WGS) reaction is a key step in all carbon-based fuel processing aimed at producing and upgrading hydrogen (*1*). For use in low-temperature fuel cells, the WGS catalysts must be nonpyrophoric, active over a wide temperature range, and stable during frequent shutdown-restart operation cycles. To meet these criteria, a reemergence of platinum-group metals has occurred in recent years, and various combinations are being evaluated as low-temperature WGS catalysts (*2*). Nanoscale ceria is the support of choice because of its high concentration of oxygen defects and stabilization of active Pt species (*2*).

The WGS reaction mechanism on Pt-CeO_2 has been debated as either involving formate intermediates (*3*) or a simple redox chemistry (*4*). Recently, Mavrikakis and co-workers showed that a carboxyl-mediated mechanism is responsible for the WGS reaction on Cu (*5*) and other metallic sites, including Pt (*6*). In both the redox and carboxyl mechanisms, the activation of H_2O, leading to the formation of the species responsible for oxidizing CO, is a kinetically important step (*7*). Furthermore, the supply of oxidizing species and the related WGS activity has been shown to be high on metals supported on reducible oxides (*8*), whereas no WGS activity has been reported for Pt supported on irreducible oxides, such as silica.

A recent key finding is that oxidized Pt (and Au) species in ceria are the catalytic sites for the WGS reaction (*2*, *9*); Pt or Au nanoparticles are spectator species. This observation has also been made for Au on Fe_3O_4 catalysts (*10*, *11*). On these oxide surfaces, nanoparticles, clusters, and atoms (ions) of Pt or Au coexist, but the chemistry takes place on the atomically dispersed $Pt^{\delta+}$ or $Au^{\delta+}$ species and involves the neighboring OH groups. Aberration-corrected high angle annular dark field (HAADF) scanning transmission electron micros-

Table 1. Physical properties and reducibility of parent and washed (deionized water–washed samples were heated to 400°C in air 4 hours) xPt-yNa-SiO_2 samples (x and y are atomic percentages.). Bulk composition was measured by inductively coupled plasma optical emission spectrometry; surface concentration, by XPS; surface [O], from CO-TPR (5% CO–He, from room temperature to 400°C, at 10°C/min); and surface [OH] from CO-TPR using only the CO_2 peak associated with the production of H_2. The XPS-measured value of surface Pt was used in calculating the [OH]/Pt ratio. Dash entries indicate nondetectable amounts, and NA, not applicable.

Sample	Bulk composition (atomic %)		Surface concentration (atomic %)		Surface [O] ($\mu mol/g_{cat}$)	Surface Na/Pt	Surface Na/O	Surface [OH]/Pt
	Pt	Na	Pt	Na				
3Na-SiO_2	0	3.0	0	4.0	500	NA	1.5:1	NA
3Na-SiO_2 washed	0	–	0	–	–	NA	–	NA
1Pt-1Na-SiO_2	1	1.0	0.3	0.9	210	3:1	0.7:1	2:1
1Pt-1Na-SiO_2 washed	1	0.7	0.4	0.5	185	1.2:1	1:1.5	2:1
1Pt-3Na-SiO_2	1	3.0	0.3	3.9	450	13:1	1.4:1	3:1
1Pt-3Na-SiO_2 washed	1	1.6	0.4	1.2	245	3:1	1:1	3:1

[1]Department of Chemical and Biological Engineering, Tufts University, Medford, MA 02155, USA. [2]Department of Chemical and Biological Engineering, University of Wisconsin, Madison, WI 53706, USA. [3]School of Engineering and Applied Sciences, Harvard University, Cambridge, MA 02138, USA.

*Present address: Cabot Corporation, 157 Concord Road, Billerica, MA 01821, USA.
†Present address: Chemistry Department, Brookhaven National Laboratory, Upton, NY 11973, USA.
‡Present address: Chemical Sciences and Engineering Division, Argonne National Laboratory, Argonne, IL 60439, USA.
§To whom correspondence should be addressed. E-mail: maria.flytzani-stephanopoulos@tufts.edu (M.F.-S.); manos@engr.wisc.edu (M.M.)